# Singlet NMR in a Case of High Molecular Symmetry

Urvashi D. Heramun, Mohamed Sabba, Christian Bengs, Gamal A. I. Moustafa, and Malcolm H. Levitt<sup>1, a)</sup>

<sup>1)</sup> School of Chemistry, University of Southampton, SO17 1BJ, UK

(Dated: August 4, 2025)

Spin-1/2 pairs support nuclear singlet and triplet states. The mean population difference between the singlet and triplet manifolds is termed singlet order. In suitable circumstances, nuclear singlet order is highly resistant to several relaxation mechanisms, displaying a decay time constant  $T_S$  which may greatly exceed the time constant  $T_1$  for the equilibration of nuclear magnetization. We explore the nuclear singlet relaxation of an isotopologue of squarate in a high-pH aqueous solution. The 1,3- $^{13}$ C<sub>2</sub>-isotopologue of squarate exists as a minority species of 1- $^{13}$ C<sub>1</sub>-squarate. This isotopologue has a high degree of molecular symmetry.  $^{18}$ O-enrichment is used to generate secondary isotope shifts of the  $^{13}$ C resonances, providing access to  $^{13}$ C<sub>2</sub> double-quantum coherence and  $^{13}$ C<sub>2</sub> singlet order. The  $^{13}$ C signals from the 1,2- $^{13}$ C<sub>2</sub> and 1,3- $^{13}$ C<sub>2</sub> species are selected using geometric double-quantum filtration, and the double-quantum coherence converted to singlet order and back again using customized double-quantum-to-singlet (DQ2S) and singlet-to-double-quantum (S2DQ) pulse sequences. We report  $^{13}$ C<sub>2</sub> singlet lifetime measurements for 1,3- $^{13}$ C<sub>2</sub>-squarate in a high-pH aqueous solution, in high magnetic field.

### I. INTRODUCTION

In high-field nuclear magnetic resonance (NMR), the nuclear spins becomes slightly polarized when the sample is allowed to reach thermal equilibrium in a strong magnetic field. The time constant for the establishment of thermal nuclear spin polarization is denoted  $T_1$ . However, this time constant does not always set a fundamental limit on the lifetime of nuclear spin order. In some circumstances, long-lived states (LLS) have been identified which, in suitable circumstances and in some nuclear spin systems, have much longer lifetimes than  $T_1^{1-33}$ . One prominent example of a LLS is the singlet order of pairs of coupled spins-1/2, defined as the population imbalance between the singlet state of the spin pair with total nuclear spin I=0, and that of the triplet manifold with I=1, defined as follows:

$$|S_{0}\rangle = (|\alpha\beta\rangle - |\beta\alpha\rangle)/\sqrt{2},$$

$$|T_{+1}\rangle = |\alpha\alpha\rangle,$$

$$|T_{0}\rangle = (|\alpha\beta\rangle + |\beta\alpha\rangle)/\sqrt{2},$$

$$|T_{-1}\rangle = |\beta\beta\rangle.$$
(1)

Here  $\alpha$  and  $\beta$  denote the two spin angular momentum projections  $\pm(\hbar/2)$  along an external axis, and the subscripts  $M_I \in \{+1,0,-1\}$  refer to the value of the magnetic spin quantum number.

A prerequisite for the existence of long-lived states is the existence of consistent symmetry in the fluctuating spin Hamiltonian that drives the relaxation process. This means that the fluctuating Hamiltonian is always invariant under one or more permutation operations or geometrical transformations, despite its stochastic time-

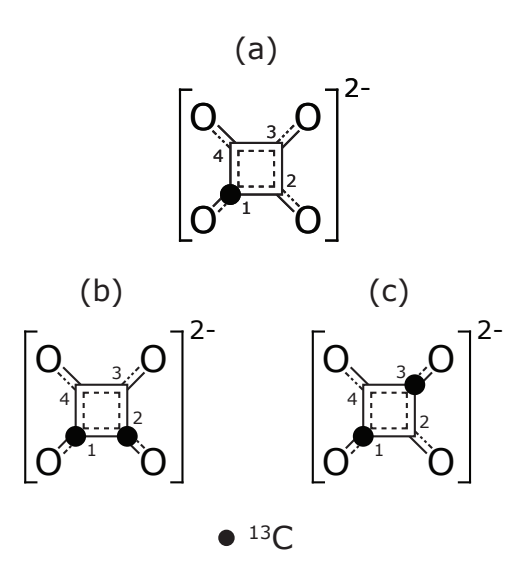


Figure 1. Molecular structures of the squarate dianion, containing one or two  $^{13}\mathrm{C}$  atoms, indicated by filled circles. The squarate dianion is the dominant species in high-pH solutions of squaric acid. (a)  $^{13}\mathrm{C}_1\text{-squarate}$ ; (b)  $1,2\text{-}^{13}\mathrm{C}_2\text{-squarate}$ , as studied in ref.  $^{25}$ ; (c)  $1,3\text{-}^{13}\mathrm{C}_2\text{-squarate}$ . In the current work, double-quantum filtering is used to suppress the  $^{13}\mathrm{C}$  NMR signals of  $^{13}\mathrm{C}_1\text{-squarate}$ , allowing the observation of signals from the  $1,2\text{-}^{13}\mathrm{C}_2\text{-squarate}$  and  $1,3\text{-}^{13}\mathrm{C}_2\text{-squarate}$  isotopologues.

dependence. Consider, for example, an ensemble of isolated spin-1/2 pairs, where the two spins  $I_j$  and  $I_k$  in each pair only experience their mutual magnetic dipole-dipole coupling. Fluctuations in the orientation and magnitude of the dipole-dipole coupling tensor generate nuclear spin relaxation. The Hamiltonian  $\mathcal{H}_{jk}^{\mathrm{DD}}$  describing the mutual dipole-dipole interaction of the two spins may be written as follows:

$$\mathcal{H}_{jk}^{\mathrm{DD}}(t) = \mathbf{I}_{j} \cdot \mathbf{D}_{jk}(t) \cdot \mathbf{I}_{k}, \tag{2}$$

<sup>&</sup>lt;sup>2)</sup>Department of Chemistry and Materials Science Division, Lawrence Berkeley National Laboratory, University of California Berkeley, Berkeley, California 94720, USA

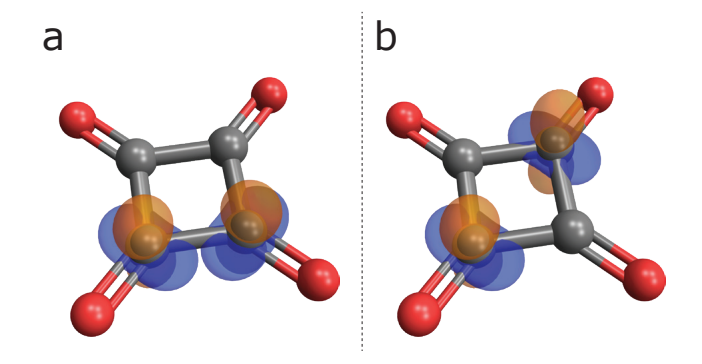


Figure 2. Ovaloid representations<sup>35,36</sup> of the <sup>13</sup>C CSA tensors, superimposed on the structure of the squarate dianion  $(C_2O_4^{2-})$ . (a) The <sup>13</sup>C CSA tensors of  $1,2^{-13}C_2$ -squarate. (b) The <sup>13</sup>C CSA tensors of  $1,3^{-13}C_2$ -squarate. Further details on the tensor calculations are given in the Supporting Information.

where the dipole-dipole coupling tensor  $\mathbf{D}_{jk}$  is symmetric. Hence, this Hamiltonian is invariant, at all times, to the permutation operation exchanging the two spins:

$$(jk)\mathcal{H}_{jk}^{\mathrm{DD}}(jk)^{\dagger} = \mathcal{H}_{jk}^{\mathrm{DD}}.$$
 (3)

Here (jk) denotes the simple swap operator that exchanges the spin  $I_j$  with the spin  $I_k$ . Even though  $\mathcal{H}^{\mathrm{DD}}_{jk}$  fluctuates strongly in time (for a molecule in solution), the symmetry property in Equation 3 is always preserved. The singlet and triplet states in Equation 1 span different irreducible representations of the permutation group  $\mathcal{G} = \{(), (jk)\}$ , where () denotes the identity<sup>34</sup>. Hence, all matrix elements of  $\mathcal{H}^{\mathrm{DD}}_{jk}$  between the singlet and triplet states vanish. As a result, the population difference between the singlet and triplet manifolds is immune to relaxation, under these idealised conditions. The same result is obtained by considering the spin quantum numbers I=0 and I=1 for the singlet and triplet states respectively, and the description of  $\mathcal{H}^{\mathrm{DD}}_{jk}$  as a sum of rank-2 irreducible spherical tensor operator components<sup>5</sup>.

In realistic circumstances, perfect permutation invariance is not displayed by all the interactions responsible for spin relaxation, leading to a finite lifetime for long-lived singlet order. In particular, interactions such as the chemical shift anisotropy, and dipolar interactions with additional spins in the same molecule, are not fully permutation-symmetric, except in special cases of particular nuclear locations within molecules of high symmetry.

For example, consider the highly symmetrical squarate dianion  $(C_4O_4^{2-})$ , illustrated in Figure 1. The doubly- $^{13}$ C labelled species 1,2- $^{13}$ C<sub>2</sub>-squarate, shown in Figure 1(b), was previously synthesised and studied in solution by  $^{13}$ C singlet NMR<sup>25</sup>.  $^{18}$ O enrichment was used to induce a very small chemical shift difference between the two  $^{13}$ C sites, giving experimental access to the long-lived singlet order.

The singlet decay time constant  $T_S$  was previously shown to be strongly pH-dependent, due to chemical ex-

change between the protonated forms<sup>25</sup>. In the current work, we concentrate on the high-pH regime, where the squarate dianion is the sole species present in significant concentration.

Since the two <sup>13</sup>C sites in 1,2-<sup>13</sup>C<sub>2</sub>-squarate are related by a  $\pi/2$  rotation about the molecular  $C_4$  symmetry axis, their CSA tensors have the same eigenvalues (principal values). However, the eigenvectors (principal axes) of the two CSA tensors are not identical, also being related by a  $\pi/2$  rotation. This is illustrated in Figure 2(a), which shows the calculated <sup>13</sup>C CSA tensors of 1,2-<sup>13</sup>C<sub>2</sub>-squarate, represented by ovaloids<sup>35,36</sup>, superimposed on the molecular structure. Since the two <sup>13</sup>C tensors have different orientations, the difference between the two CSA tensors, which contributes to the singlet  $relaxation^{10,12}$ , does not vanish. Hence, although the squarate molecule itself is highly symmetrical, the two <sup>13</sup>C nuclei in 1,2-<sup>13</sup>C<sub>2</sub>-squarate are not in sufficiently symmetrical positions to suppress the CSA contribution to singlet relaxation. A similar conclusion applies to the spin-rotation mechanism<sup>9</sup>.

The situation in the  $1,3^{-13}C_2$ -squarate isotopologue of Figure 1(c) is more favourable with respect to the suppression of CSA relaxation. The two <sup>13</sup>C sites of 1,3-<sup>13</sup>C<sub>2</sub>-squarate are related by a molecular *inversion* operation. In general any two molecular sites related by inversion have identical CSA and spin-rotation tensors<sup>37</sup>, as shown in Figure 2(b). Hence the CSA and spinrotation contributions to the <sup>13</sup>C<sub>2</sub> singlet relaxation of 1,3-13C<sub>2</sub>-squarate is completely eliminated, within the approximation of rigid molecular geometry. Furthermore, a molecule of 1,3-<sup>13</sup>C<sub>2</sub>-squarate contains no other intramolecular relaxation sources, since the <sup>12</sup>C, <sup>16</sup>O and <sup>18</sup>O isotopes all have nuclear spin I = 0. This implies that 1,3-<sup>13</sup>C<sub>2</sub>-squarate might be a near-ideal vehicle for the storage of long-lived spin order in solution. The contributions to singlet relaxation are restricted to relatively inefficient intermolecular mechanisms, and to residual intramolecular perturbations – caused by temporary geometrical fluctuations, very infrequent protonation events (at high pH), and the possible minor influence of <sup>18</sup>O substitution on the interaction tensors.

A molecular system with approximate local inversion symmetry was previously engineered in the form of a  $^{13}\mathrm{C}_2$ -labelled naphthalene derivative, and displayed an exceptionally long singlet relaxation time  $T_S$  of more than 1 hour in a degassed non-viscous solvent in low magnetic field  $^{18}$ . However, that molecular system also contained several spin I=1 deuterium nuclei, which could contribute to residual relaxation processes. The  $1,3^{-13}\mathrm{C}_2$ -squarate system of Figure 2(b) possesses near-ideal inversion symmetry without any other magnetisation sources within the same molecule, and is also compatible with an aqueous environment – albeit at high pH.

However, a series of technical obstacles lies in the way of accessing and measuring the  ${}^{13}\mathrm{C}_2$  singlet order of 1,3- ${}^{13}\mathrm{C}_2$ -squarate. The first of these is chemical: Although synthetic routes exist for 1- ${}^{13}\mathrm{C}_1$ -squarate and 1,2- ${}^{13}\mathrm{C}_2$ -

squarate<sup>25</sup>, the same is not currently true for the 1,3- $^{13}\mathrm{C}_2$  isotopologue. Rather than develop the necessary synthetic chemistry, we chose to work with the singly  $^{13}\mathrm{C}$ -labelled isotopomer, using the  $\sim 1.1\%$  natural abundance of  $^{13}\mathrm{C}$  to provide the second  $^{13}\mathrm{C}$  site. This provides simultaneous access to the 1,2- $^{13}\mathrm{C}_2$  and 1,3- $^{13}\mathrm{C}_2$ -squarate isotopologues, at the expense of relatively poor signal strength.

The second obstacle is that access to the potentially long-lived  $^{13}\mathrm{C}_2$  singlet order of  $1,3^{-13}\mathrm{C}_2$ -squarate requires breaking the chemical equivalence of the two  $^{13}\mathrm{C}$  sites, ideally with only a minimum disturbance to the highly symmetrical molecular structure. This condition may be satisfied by substituting one or more  $^{16}\mathrm{O}$  atoms by the heavier  $^{18}\mathrm{O}$  isotope, which also has nuclear spin I=0. The substitution of one isotope by another of different mass causes small secondary isotope shifts in the chemical shift values  $^{38-44}$ . This approach was used previously in the singlet NMR of  $^{13}\mathrm{C}_2$ -oxalate  $^{15}$ ,  $1,2^{-13}\mathrm{C}_2$ -squarate  $^{25}$ , and the  $^{103}\mathrm{Rh}_2$  singlet NMR of dirhodium paddlewheel complexes  $^{32}$ .

The third obstacle is that the small  $^{13}\mathrm{C}$  signals from the minor  $^{13}\mathrm{C}_2$  isotopologues of the singly- $^{13}\mathrm{C}$ -labelled species are readily obscured by the much larger signals from the abundant  $^{13}\mathrm{C}_1$  species. This obstacle may be overcome by using double-quantum filtration, which is widely used for selective detection of  $^{13}\mathrm{C}$  signals from  $^{13}\mathrm{C}_2$  species, with suppression of those from  $^{13}\mathrm{C}_1$  species<sup>45</sup>.

In the current case, double-quantum filtering of <sup>13</sup>C<sub>2</sub> signals encounters a fourth obstacle. The standard techniques for double-quantum excitation in solution NMR require a large chemical shift difference between the coupled spins, relative to the *J*-coupling between them (the "weakly coupled" case)<sup>45</sup>. However, the <sup>18</sup>O-induced secondary <sup>13</sup>C isotope shifts are small, and usually generate <sup>13</sup>C<sub>2</sub> spin-pair systems in the "near-equivalence" or "extreme strong coupling" limit (the chemical shift frequency difference is much smaller than the J-coupling)<sup>11</sup>. The standard INADEQUATE pulse sequence<sup>45</sup> has very poor efficiency in the near-equivalence regime. Although the pulse sequence intervals may be extended to deal with strong coupling<sup>46</sup>, this approach leads to a much longer pulse sequence duration and hence enhanced relaxation losses.

Fortunately, a solution to the problem of double-quantum excitation in the regime of extreme strong coupling is at hand. The technique known as geometric double-quantum excitation (GeoDQ) exploits the geometric Aharanov-Anandan quantum phase to generate double-quantum coherences with high efficiency in near-equivalent spin-1/2 pairs<sup>47</sup>. In the work described below, we used GeoDQ to selectively detect the small  $^{13}{\rm C}_2$  signals of  $^{13}{\rm C}_1$ -labelled squarate, while suppressing the much larger signals from isolated  $^{13}{\rm C}$  nuclei. The double-quantum coherences were converted into singlet order by further manipulations, allowing study of the  $^{13}{\rm C}_2$  long-lived state in the minor isotopologues of  $^{18}{\rm O}\text{-enriched}$ 

 $^{13}\mathrm{C}_1$ -squarate.

In the rest of the paper we describe a series of <sup>13</sup>C NMR observations on an aqueous solution of <sup>18</sup>O-enriched 1-<sup>13</sup>C-squarate. A rich spectral pattern is observed due to the pH-dependent <sup>18</sup>O-induced secondary isotope shifts of the  $^{13}\mathrm{C}$  resonances and the many possible  $^{18}\mathrm{O}$ isotopologues. As described below, the evidence indicates that the pH-dependence of the <sup>18</sup>O-induced <sup>13</sup>C isotope shifts is not only due to the <sup>18</sup>O-induced perturbations of the vibrational wavefunctions, but also perturbations of the acid-base equilibria by the substitution of <sup>18</sup>O for <sup>16</sup>O. We demonstrate the successful implementation of geometric double-quantum excitation to selectively detect the <sup>13</sup>C NMR signals from <sup>18</sup>O isotopologues of 1,2- $^{13}\text{C}_2$  and  $1{,}3^{-13}\text{C}_2$ -squarate. This made it possible to determine the <sup>13</sup>C<sub>2</sub> singlet lifetimes of both <sup>13</sup>C<sub>2</sub> isotopologues of the squarate di-anion, in a high magnetic field.

# II. MATERIALS AND METHODS

# A. Sample Preparation

The samples consisted of 4.6 mg of 1-<sup>13</sup>C-squaric acid, dissolved in 400  $\mu$ L of a 1:1 mixture of  $H_2^{18}O:D_2^{16}O$  to make up a 0.1 M solution. The isotopic purity of  $H_2^{18}O$ was 97.1 %. The solutions were incubated at 80°C for two hours, to allow the  ${}^{16}O/{}^{18}O$  exchange process to reach a dynamic equilibrium. Samples with differing pH values were prepared by step-wise addition of a 2 M solution of sodium hydroxide. For each instance, the volume did not exceed 65  $\mu$ L, and therefore any effects on sample concentration were deemed negligible. The pH measurements were carried out with a Hamilton SpinTrode pH electrode (www.hamiltoncompany.com). The calibration of the pH meter was verified over the full pH range, using standard buffers. When degassing is indicated, this was achieved by a standard freeze-pump-thaw procedure under an inert atmosphere, for ten total cycles.

### B. NMR Instrumentation

The solution-state NMR experiments were carried out on a Bruker Neo Avance 400 MHz system equipped with a 5 mm Bruker BBO probe, and a Bruker Neo Avance 700 MHz system equipped with a Bruker TCI prodigy 5 mm cryoprobe. The 90° pulse length  $\tau_{90}$  was optimised to  $9.15 \pm 0.1~\mu s$  at 400 MHz, and  $12.75 \pm 0.1~\mu s$  at 700 MHz.

### III. RESULTS

### A. <sup>13</sup>C NMR spectra

The <sup>13</sup>C spectrum of the <sup>18</sup>O-enriched 1-<sup>13</sup>C-squarate solution takes the form of 12 closely-spaced peaks, as

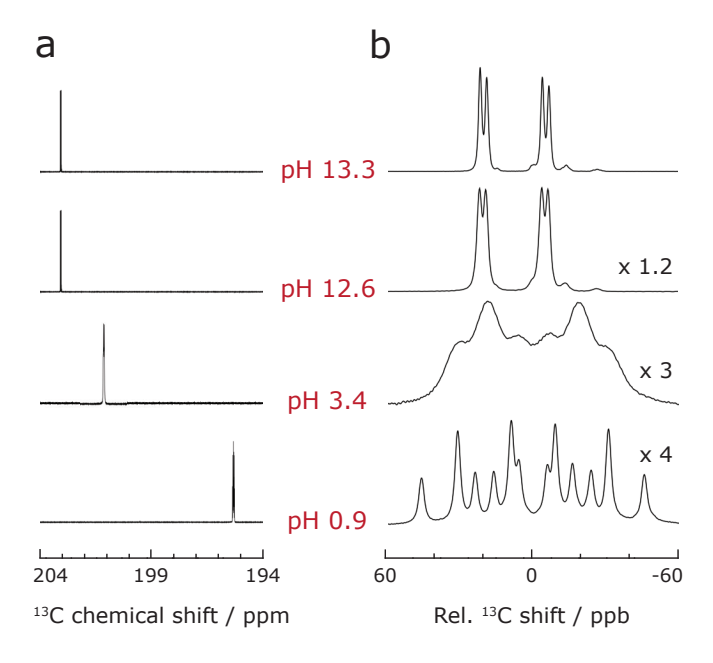


Figure 3. (a) Variation in the  $^{13}\mathrm{C}$  chemical shift positions as a function of pH for samples of  $^{18}\mathrm{O}$ -enriched  $^{13}\mathrm{C}_1$ -squaric acid dissolved in 1:1  $\mathrm{H_2}^{18}\mathrm{O}$ :D<sub>2</sub> $^{16}\mathrm{O}$ . Each spectrum was acquired for 200 transients at 9.4 T and 298 K. (b) Expansion of the relevant spectral region for each pH point shown, spanning 120 ppb. The chemical shift scale at pH 0.9 is centred around 195.32 ppm, 201.12 ppm at pH 3.4, and 203.05 ppm at pH 12.6 and pH 13.3. The vertical scales are given with respect to the pH 13.3 spectrum.

shown in Figure 3(b). The mean chemical shift of the multiplet shifts downfield (i.e. high values of chemical shift  $\delta$ ) as the pH is increased, as shown in Figure 3(a). The mean  $^{13}{\rm C}$  chemical shift changes by  $\sim +7.7\,{\rm ppm}$  when the pH is increased from 0.9 to 13.3.

The pH-dependence of the  $^{13}\mathrm{C}$  chemical shift is due to the dynamic equilibrium of the squarate dianion with the conjugate acids mono-hydrogen squarate ( $\mathrm{C_2O_4H^-}$ ) and the di-protonated neutral species squaric acid ( $\mathrm{C_2O_4H_2}$ ), as shown in Figure 4. The observed  $^{13}\mathrm{C}$  chemical shift is a population-weighted average of the  $^{13}\mathrm{C}$  shifts of the rapidly exchanging species in solution. This leads to a strong pH-dependence of the mean  $^{13}\mathrm{C}$  chemical shift, as shown in Figure 3(a).

Figure 3(b) shows expanded views of the 12-peak multiplet as a function of pH. Note that the frequency axes of the four spectra in Figure 3(b) are centred at different chemical shift values, as described in the caption. The 12 multiplet components are quite well-resolved at pH=0.9, with the multiplet pattern spanning almost 50 ppb. The spectrum at pH=3.4 is strongly broadened. At high pH values the  $^{13}{\rm C}$  spectrum takes the form of two well-separated doublets, flanked by small additional features which are attributed to minor isotopologues with two  $^{13}{\rm C}$  nuclei, as discussed in detail below.

As is clear from Figure 3(b), the <sup>18</sup>O-induced secondary <sup>13</sup>C isotope shifts are strongly pH-dependent.

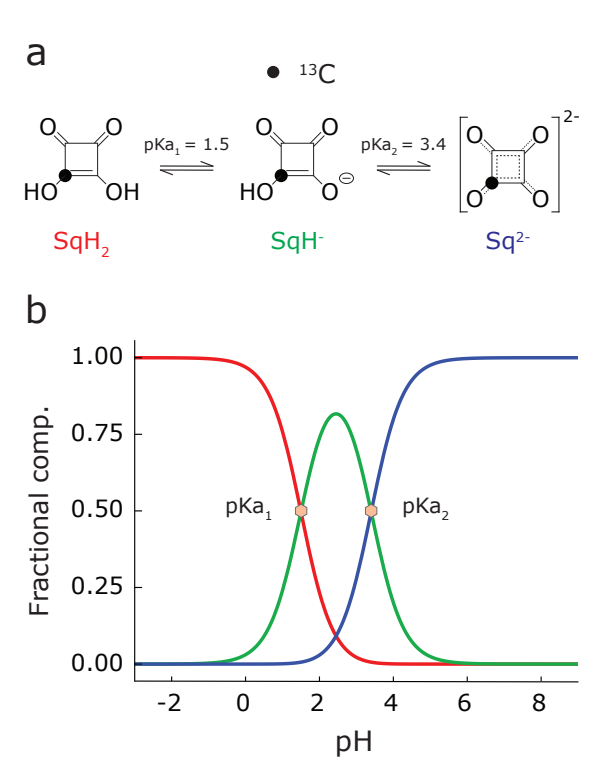


Figure 4. (a) Dynamic equilibrium displayed by  $^{13}C_1$ -squaric acid in solution. The diprotic squaric acid  $SqH_2$  (red) is most abundant below  $pKa_1 = 1.5$ , while the squarate dianion  $Sq^{2-}$  (blue) dominates beyond  $pKa_2 = 3.4$ . Between the two extremes is the singly-protonated species hydrogen squarate  $SqH^-$  (green). (b) Fractional composition diagram showing the distribution of the various species of squaric acid at different pH values. Each pKa value equals the pH at the corresponding half-equivalence point.

There are two relevant mechanisms for the secondary isotope shifts:

- 1. Vibronic mechanism. Observed chemical shifts are averages over vibrational wavefunctions; since vibrational wavefunctions are modified by changing the mass of the participating atoms, isotopic substitution slightly modifies the vibrationally-averaged chemical shifts. This mechanism has been documented thoroughly<sup>38–42</sup>. The theory is well-developed, even including relativistic effects<sup>43,44</sup>. Vibronic secondary isotope shifts often become smaller in magnitude as the number of bonds separating the participating atoms increases. However, this is not always the case, as is shown below.
- 2. Dynamic mechanism. For chemically exchanging systems, in the fast exchange regime, the observed chemical shifts are population-weighted averages over the chemical shifts of the relevant chemical species. Replacement of <sup>16</sup>O by <sup>18</sup>O modifies the equilibrium concentrations of the exchanging species, for example by changing the zero-point energy of O-H bond vibrations, effectively modifying

the acidity of the affected -OH group<sup>48,49</sup>. Since the observed chemical shift depends on the equilibrium concentrations of the exchanging species, isotopic substitution can lead to chemical shift changes, even remote from the site of isotopic substitution. This effect, is called here the *dynamic* isotope shift mechanism. In suitable cases, dynamic isotope shifts may be much larger than vibronic isotope shifts, may be observed much further from the site of isotopic substitution than vibronic isotope shifts, and may have the opposite sign to vibronic shifts. So far, the dynamic isotope shift mechanism has not been as thoroughly examined as the vibronic mechanism, although its importance has been identified in some cases 42,48-51. Some reports of unusually large and unexplained isotope shifts may probably be attributed to the dynamic mechanism $^{52}$ .

In the current system, the  $^{18}\text{O}$ -induced secondary  $^{13}\text{C}$  isotope shifts are caused by a superposition of the vibronic and dynamic mechanisms. A detailed analysis is deferred to a future report.

In the following discussion, the secondary isotope shifts are described by the following convention, as used in recent papers<sup>15,25</sup>:

$$^{n}\Delta X(h) = \delta_{X}(h) - \delta_{X}(l), \tag{4}$$

Here  $\Delta$  represents the chemical shift difference induced by substitution, X the nucleus being observed, h the heavier isotope, l the lighter isotope, and n the number of chemical bonds separating X and h. This convention is intuitive since it indicates the change in chemical shift when the most common isotope is replaced by a heavier one, although some literature uses the opposite sign<sup>41</sup>.

# 1. 13C spectrum at pH 0.9

A detailed view of the  $^{13}\mathrm{C}$  spectrum of the  $^{18}\mathrm{O}$ -enriched  $1^{-13}\mathrm{C}$ -squarate solution at pH=0.9 is shown in Figure 5, together with the assignments of the 12 peaks to the  $^{18}\mathrm{O}$  isotopologues. Because of the molecular symmetry, some isotopologues, such as  $1^{-13}\mathrm{C}$ ,  $2^{-18}\mathrm{O}$ -squarate (peak 2), are twice as probable as some others, such as

Table I. Experimentally measured secondary isotope shifts for  $^{18}\text{O-enriched}$   $^{13}\text{C}_1$ -squarate at pH 0.9 (Figure 5), in a magnetic field of 9.4 T and a sample temperature of 298 K. The isotope shift convention is given in Equation 4.

<sup>13</sup> C Isotope Shift	${\bf Value\ /ppb}$
$^{1}\Delta^{13}C(^{18}O)$	$-40.1 \pm 0.5$
$^{2}\Delta^{13}C(^{18}O)$	$-14.9 \pm 0.5$
$^{3}\Delta^{13}C(^{18}O)$	$-22.1 \pm 0.5$

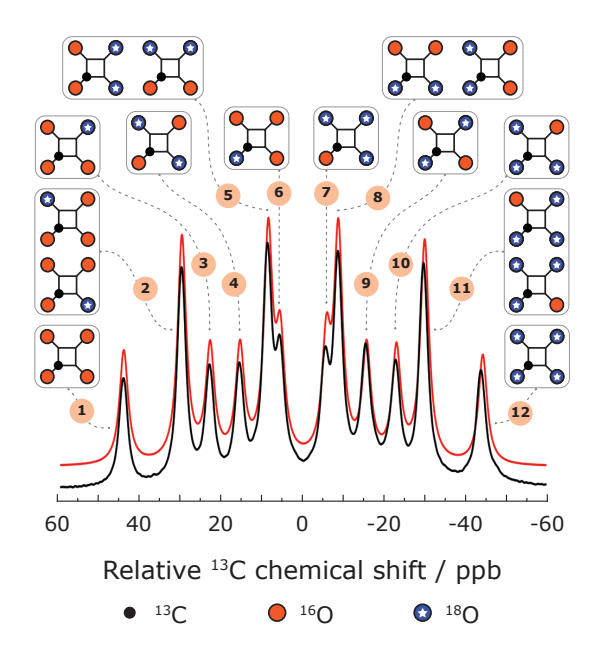


Figure 5. The isotopologues of  $^{18}\text{O-enriched}$   $^{13}\text{C}_1$ -squarate, and their correspondence with the  $^{13}\text{C}$  spectrum at pH 0.9. The filled black circles denote  $^{13}\text{C}$  atoms. The filled orange circles denote  $^{16}\text{O}$  atoms, while the blue stars denote  $^{18}\text{O}$  atoms. The experimental spectrum at 9.4 T (black, 512 scans), is compared with a simulation of the spectrum (red). The  $^{13}\text{C}$  chemical shift scale is centred at 195.32 ppm.

 $1^{-13}$ C,  $3^{-18}$ O-squarate (peak 3). Peak 2 therefore has twice the intensity of peak 3. The probability of a given isotopologue is called here the *statistical weight*. The isotopologue  $1^{-13}$ C,  $2^{-18}$ O-squarate has twice the statistical weight of the isotopologue  $3^{-18}$ O-squarate.

Table I displays the set of  $^{18}\text{O-induced}$   $^{13}\text{C}$  secondary isotope shifts which is consistent with the observed spectrum at pH 0.9. A simulation of the spectrum, using the isotope shifts in Table I and the statistical weights of the isotopologues, is also shown in Figure 5. This simulation assumes that the secondary isotope shifts are additive, i.e. the secondary isotope shift of a  $^{13}\text{C}$  nucleus which is one bond away from one  $^{18}\text{O}$  atom and two bonds away from a second  $^{18}\text{O}$  atom experiences a secondary isotope shift of  $^1\Delta^{13}\text{C}(^{18}\text{O}) + ^2\Delta^{13}\text{C}(^{18}\text{O}),$  and similarly for all the other isotopologues. The agreement with the experimental spectrum is good.

Note that the secondary isotope shifts in table I do not show a monotonic dependence on the number of bonds n separating the atoms, the two-bond shifts being smaller in magnitude than the three-bond shifts. All isotope shifts are negative, meaning that the substitution of  $^{16}{\rm O}$  by the heavier  $^{18}{\rm O}$  isotope leads to a decrease in the  $^{13}{\rm C}$  chemical shift  $\delta$ , i.e. a "high-field" shift. The peak of the  $^{16}{\rm O}_4$  isotopologue therefore has the highest  $\delta$  value, and appears on the extreme left of the  $^{13}{\rm C}$  multiplet, while the peak of the  $^{18}{\rm O}_4$  isotopologue appears on the extreme right. We are confident that no other combinations of isotope shifts matches the observed spectra.

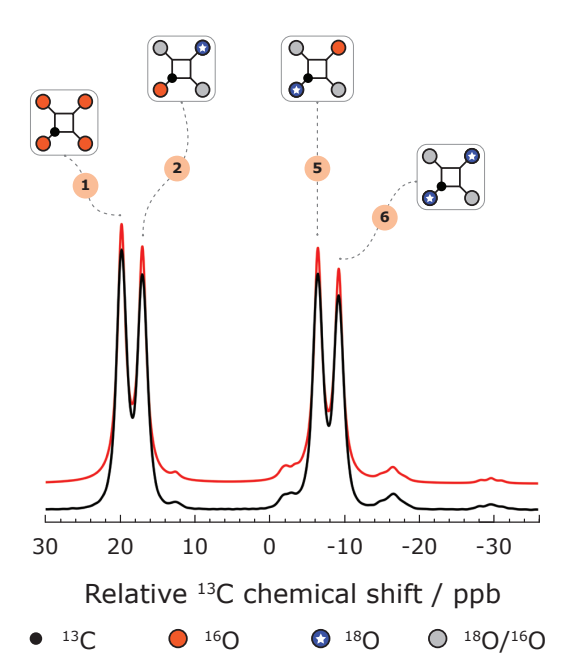


Figure 6. The  $^{18}{\rm O}$  isotopologues of  $^{13}{\rm C}_1$ -squarate, and their correspondence with the  $^{13}{\rm C}$  spectrum at pH 13.3. The filled black circles denote  $^{13}{\rm C}$  atoms. The filled orange circles denote  $^{16}{\rm O}$  atoms, while the blue stars denote  $^{18}{\rm O}$  atoms. Filled grey circles denote oxygen atoms which may be either  $^{16}{\rm O}$  or  $^{18}{\rm O}$ , since the two-bond isotope shift  $^2\Delta^{13}{\rm C}(^{18}{\rm O})$  is negligible (see table II), the isotopic nature of these oxygen atoms does not affect the  $^{13}{\rm C}$  spectrum. The experimental spectrum at 9.4 T (black, 512 scans), is compared with a simulation of the spectrum (red). The  $^{13}{\rm C}$  chemical shift scale is centred at 203.05 ppm.

### 2. 13C spectrum at pH 3.4

The  $^{13}$ C spectrum at pH  $\simeq 3.4$  is shown in Figure 3(b). The spectral peaks are relatively broad, presumably because the protonation and deprotonation events occur, at this pH value, on a similar time scale to the inverse of the exchange-induced changes in the  $^{13}$ C resonance frequency. This spectrum was not analysed further.

# 3. <sup>13</sup>C spectrum at pH 13.3

At high pH values, the <sup>13</sup>C spectrum of the <sup>18</sup>O-enriched 1-<sup>13</sup>C-squarate solution displays four strong peaks, arranged as two well-separated doublets. The assignments of the four <sup>13</sup>C peaks to the <sup>18</sup>O isotopologues of 1-<sup>13</sup>C-squarate is shown in Figure 6. The <sup>18</sup>O-induced secondary isotope shifts at high pH are given in Table II. At this pH value, only the deprotonated squarate dianion is present in appreciable concentration. Hence, the high-pH <sup>13</sup>C isotope shifts may be attributed solely to the vibronic mechanism.

Surprisingly, the two-bond secondary isotope shift  $^2\Delta^{13}C(^{18}O)$  is found to be indistinguishable from zero,

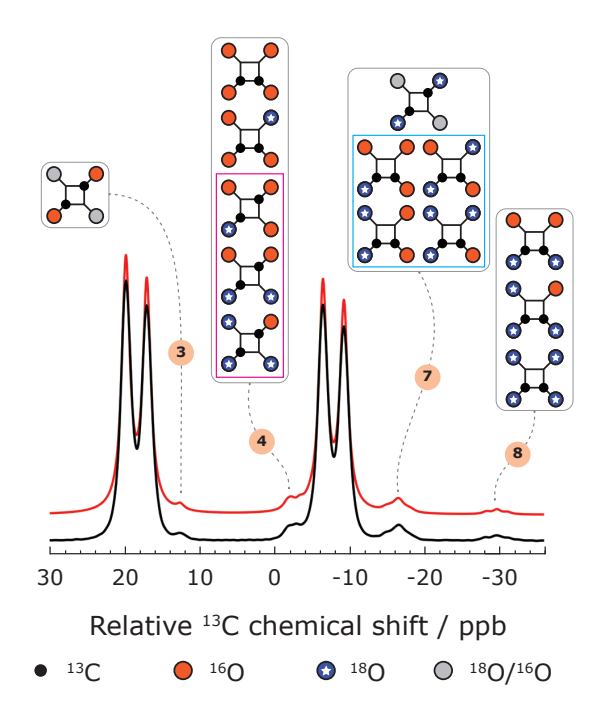


Figure 7. The  $^{18}{\rm O}$  isotopologues of  $^{13}{\rm C}_2\text{-squarate},$  and their correspondence with the  $^{13}{\rm C}$  spectrum at pH 13.3. The filled black circles denote  $^{13}{\rm C}$  atoms. The filled orange circles denote  $^{16}{\rm O}$  atoms, while the blue stars denote  $^{18}{\rm O}$  atoms. Filled grey circles denote oxygen atoms which may be either  $^{16}{\rm O}$  or  $^{18}{\rm O}$ . The experimental spectrum at 9.4 T (black, 512 scans), is compared with a simulation of the spectrum (red). The  $^{13}{\rm C}$  chemical shift scale is centred at 203.05 ppm.

at high pH. There is no other feasible interpretation for the two-doublet form of the high-pH  $^{13}\mathrm{C}$  spectrum. At present, the surprisingly low value of the two-bond  $^{18}\mathrm{O}$ -induced vibronic  $^{13}\mathrm{C}$  isotope shift is unexplained. This observation is possibly associated with the high symmetry of the molecule.

The high-pH spectrum also displays smaller features which are attributed to low-abundance isotopologues

Table II. Estimated values of the  $^{18}{\rm O}$  and  $^{13}{\rm C}$ -induced  $^{13}{\rm C}$  isotope shifts of  $^{18}{\rm O}$ -enriched  $^{13}{\rm C}_1$ -squarate at pH 13.3 (Figures 6 and 7) at 9.4 T and 298 K. Note the negligible magnitude of the two-bond  $^{18}{\rm O}$ -induced isotope shift  $^2\Delta^{13}{\rm C}(^{18}{\rm O})$ . The isotope shift convention is given in Equation 4.

<sup>13</sup> C Isotope Shift	Value /ppb
$^{1}\Delta^{13}C(^{18}O)$	$-25.7 \pm 0.5$
$^{2}\Delta^{13}{ m C}(^{18}{ m O})$	$0.0 \pm 0.5$
$^{3}\Delta^{13}C(^{18}O)$	$-2.7 \pm 0.5$
$^{-1}\Delta^{13}C(^{13}C)$	$-21.3 \pm 0.5$
$^{2}\Delta^{13}C(^{13}C)$	$-7.1 \pm 0.5$

Table III. First three rows: Pulse sequence parameters used for the geometric double-quantum filtration experiments at 16.4 T and 298 K for a pH 13.3 sample. Next four rows: spin system parameters deduced from the optimised values of the pulse sequence parameters, using Equations 6 to 8. The small values of  $\theta_{\rm ST}$  indicate  $^{13}{\rm C}_2$  spin pairs in the near-equivalence regime. Last row: estimated values of the  $^{13}{\rm C}^{-13}{\rm C}$  J-couplings by a range of computational chemistry methods (see Supporting Information).

Parameter	$1,2^{-13}C_2$ -sq.	$1,3^{-13}C_2$ -sq.
$\phantom{aaaaaaaaaaaaaaaaaaaaaaaaaaaaaaaaaaa$	4.53	6.21
$ au_2 \ / \mathrm{ms}$	9.06	12.42
n	20	16
$J/{ m Hz}$	$55.0 \pm 0.1$	$40.1 \pm 0.1$
$\Delta \delta \ / { m ppb}$	$5.8 \pm 0.1$	$5.8 \pm 0.1$
$\Omega/(2\pi)~/{ m Hz}$	$55.2 \pm 0.1$	$40.3 \pm 0.1$
$ heta_{ m ST}/^\circ$	$4.2 \pm 0.2$	$5.8 \pm 0.2$
$J_{ m calc} \ /  m Hz$	$56.5 \pm 0.5$	$47.8 \pm 0.5$

containing pairs of  $^{13}\mathrm{C}$  nuclei. The assignments of these peaks to sets of isotopologues are shown in Figure 7, together with a simulation of the spectrum using the isotope shift values in Table II. The  $^{13}\mathrm{C}$  peaks of the  $^{13}\mathrm{C}_2$ -isotopologues are shifted to low  $\delta$  values ("high-field"), relative to those of the  $^{13}\mathrm{C}_1$  species, by the secondary  $^{13}\mathrm{C}$  isotope shift induced by the presence of a  $^{13}\mathrm{C}$  neighbour. The experimentally determined  $^{1}\Delta^{13}\mathrm{C}(^{13}\mathrm{C})$  and  $^{2}\Delta^{13}\mathrm{C}(^{13}\mathrm{C})$  isotope shifts are given as the last two rows of Table II. The spectral simulations assume that all secondary isotope shifts are additive.

Simulations of the spectra, using the isotope shifts in Table II and the known statistical weights of the isotopologues, are also shown in Figures 6 and 7. These simulations assume that the secondary isotope shifts are additive. In cases where there are spectral contributions from chemically-inequivalent  $^{13}\mathrm{C}_2$  pairs, the simulations included all four peaks of the corresponding AB spin system, using the predicted  $^{18}\mathrm{O}$ -induced isotope shifts for the two  $^{13}\mathrm{C}$  nuclei, and estimated values of  $J_{\mathrm{CC}}$  from computational chemistry (see Table III). The agreement with the experimental spectra is good.

There are two sets of isotopologues which are particularly interesting from the point of view of the current paper. These are the  $^{13}\mathrm{C}_2$  isotopologues for which one  $^{13}\mathrm{C}$  atom has  $^{18}\mathrm{O}$  as a directly-bonded neighbour, while the other  $^{13}\mathrm{C}$  atom has  $^{16}\mathrm{O}$  as a directly-bonded neighbour. In these cases the asymmetrical  $^1\Delta^{13}\mathrm{C}(^{18}\mathrm{O})$  secondary isotope shifts break the chemical equivalence of the two  $^{13}\mathrm{C}$  nuclei, providing access to  $^{13}\mathrm{C}_2$  singlet order

and  ${}^{13}C_2$  double-quantum coherence. 1,2- ${}^{13}C_2$ -squarate isotopologues of this type contribute to the peak cluster at position 7 in Figure 7, while the relevant  $1,3^{-13}C_2$ squarate isotopologues contribute to peak 4. Note, however, that in both cases, the relevant signals almost coincide with those from isotopologues of less interest. In the case of peak 7, the signals of interest from the  $1,2^{-13}C_2$ , 1-<sup>18</sup>O, 2-<sup>16</sup>O species almost coincide with the signals from  $1,3^{-13}C_2$ ,  $1,3^{-18}O_2$  species; In the case of peak 4, the signals from  $1,3^{-13}C_2$ ,  $1^{-18}O$ ,  $3^{-16}O$  species almost coincide with those from 1,2-<sup>13</sup>C<sub>2</sub>, 1,2-<sup>18</sup>O<sub>2</sub> species. Furthermore, in the case of 1,3-<sup>13</sup>C<sub>2</sub>-squarate, the relevant <sup>13</sup>C peaks are close in frequency to the peak from isotopologues of 1-13C, 1-18O, 3-16O-squarate, which is present in much higher abundance (peak 5 in Figure 6). In order to observe the <sup>13</sup>C spectra of the most interesting isotopologues cleanly, it is therefore necessary to suppress the overlapping signals from the less desirable ones.

### B. Double-Quantum Filtered NMR

There are several methods for selecting the NMR signals from spin-1/2 pairs, while suppressing the signals from isolated spins-1/2. The standard method is double-quantum-filtration, which has long been used for the selective detection of  $^{13}C_2$  signals  $^{45,54}$ . An alternative method is singlet-order filtration, which exploits the isotropic rotational properties of singlet order, rather than using double-quantum coherence  $^{23,55}$ , and which has been performed in  $vivo^{27,31}$ . As described in the Supplementary Information, we explored both techniques, but found the double-quantum-filtration method to be superior in the current case, for which the large  $^{13}C$  signals from the  $^{13}C_1$  isotopologues present a significant challenge.

In the cases of interest, the resonance frequency difference between the  $^{13}\mathrm{C}$  nuclei of the  $1,2^{-13}\mathrm{C}_2$  and  $1,3^{-13}\mathrm{C}_2$  squarate isotopologues is small. This leads to  $^{13}\mathrm{C}_2$  pair systems of the near-equivalent AB type. For example, in a field of 16.4 T, the  $^1\Delta^{13}\mathrm{C}(^{18}\mathrm{O})$  secondary isotope shift of  $\sim -25.7$  ppb leads to a resonance frequency change of 4.52 Hz, which is much smaller than the estimated  $^{13}\mathrm{C}$ - $^{13}\mathrm{C}$  J-couplings of 55.0 Hz for the 1,2- $^{13}\mathrm{C}_2$  isotopologues and 40.1 Hz for the 1,3- $^{13}\mathrm{C}_2$  isotopologues (see Table III).

The relevant <sup>13</sup>C<sub>2</sub> spin pairs therefore form very strongly coupled AB systems. The standard INADE-QUATE pulse sequence for double-quantum excitation<sup>45</sup> is not suitable for this coupling regime. The INADE-QUATE pulse sequence may be adapted for the strong coupling case by greatly extending the pulse sequence duration<sup>46</sup>. However, this approach leads to considerable relaxation losses.

We therefore employed the geometric double-quantum (GeoDQ) excitation procedure, which was recently shown to be effective for double-quantum excitation in near-equivalent AB spin systems<sup>47</sup>. The double-quantum ex-

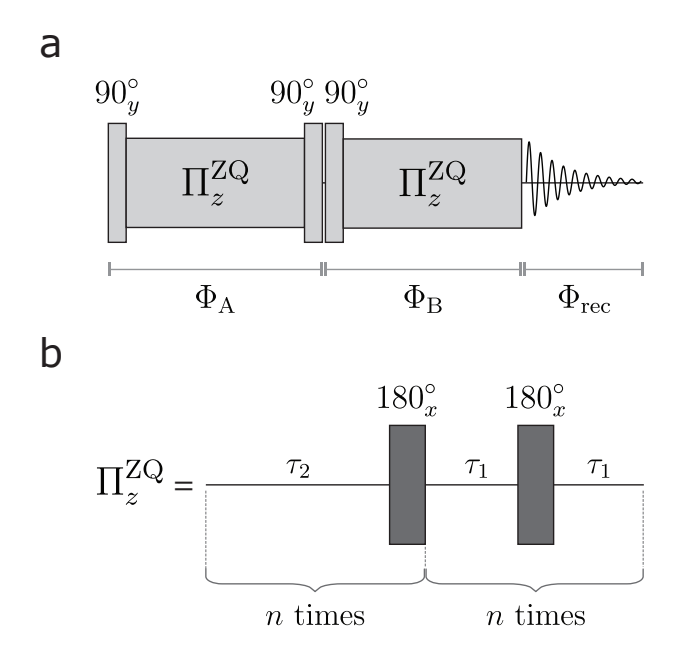


Figure 8. (a) Geometric double-quantum-filtering pulse sequence. The pulse sequence consists of two blocks, with overall phases  $\Phi_A$  and  $\Phi_B$ , which are cycled together with the receiver phase  $\Phi_{rec}$  in order to select signals passing through  $(\pm 2)$ -quantum coherence between blocks A and B. The double-quantum excitation block A consists of two  $\pi/2$  pulses bracketing a sequence labelled  $\Pi_z^{\text{ZQ}}$ , that generates a rotation through the angle  $\pi$  about the z-axis of the zero-quantum space (Equation 5). The double-quantum reconversion block B consists of a single  $\pi/2$  pulse followed by an identical  $\Pi_z^{\rm ZQ}$ sequence. The phases of the blocks are cycled as an overall four-step cycle:  $\Phi_{\rm A} = \{0,0,0,0\}, \ \Phi_{\rm B} = \{0,\pi/2,\pi,3\pi/2\}$  and  $\Phi_{\rm rec} = \{0,3\pi/2,\pi,\pi/2\}.$  (b) Each  $\Pi_z^{\rm ZQ}$  sequence consists of two elements, each of which is repeated n times, before proceeding to the next element. The first element consists of an interval  $\tau_2$  followed by a  $\pi$  pulse, with the delay-pulse sequence repeated n times. The second element consists of a delay  $\tau_1$ , a  $\pi$  pulse, and another delay  $\tau_1$ , with the delay-pulsedelay sequence repeated n times. The darker colour indicates a composite  $180^{\circ}$  pulse<sup>53</sup>. Theoretical expressions for  $\tau_1$ ,  $\tau_2$ and n are given in Equation 8. The parameters used in the experiments are given in Table III.

citation procedure is shown in Figure 8, and employs two  $\pi/2$  pulses bracketing a sequence denoted  $\Pi_z^{\rm ZQ}$ , which leads to an effective  $\pi$  rotation about the z-axis of the zero-quantum subspace spanned by the singlet state  $|S_0\rangle$  and the central triplet state  $|T_0\rangle$  of the strongly-coupled AB system (Equation 1). The propagator for this sequence, in the basis of singlet and triplet states (Equation 1), is given by:

$$\Pi_z^{\text{ZQ}} = \begin{pmatrix} -i & 0 & 0 & 0 \\ 0 & 1 & 0 & 0 \\ 0 & 0 & +i & 0 \\ 0 & 0 & 0 & 1 \end{pmatrix}.$$
(5)

The  $\Pi_z^{\rm ZQ}$  sequence inscribes a cyclic "spherical lune"

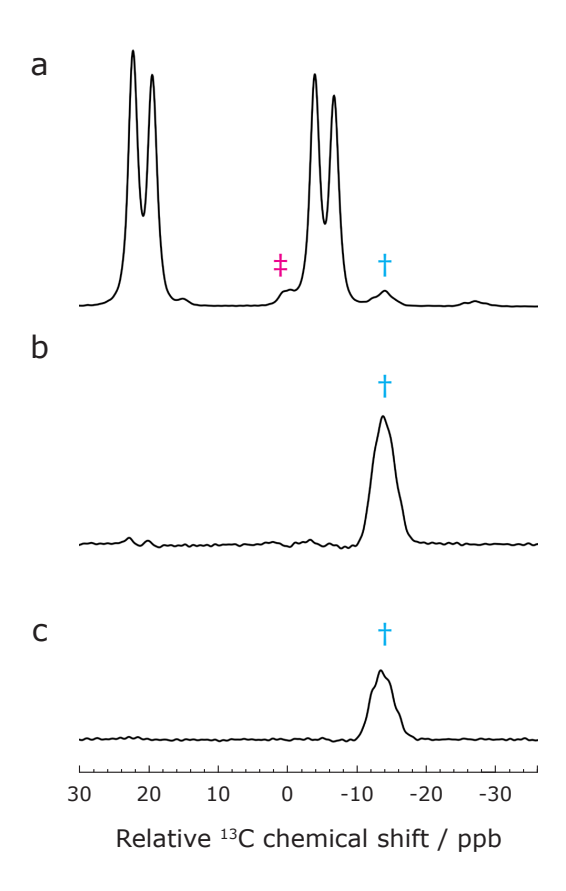


Figure 9. Selective  $^{13}$ C NMR of 1,2- $^{13}$ C<sub>2</sub>-squarate. All spectra are for a solution of  $^{13}$ C<sub>1</sub> squarate at pH 13.3 and 298 K. The chemical shift scale is centred at 203.05 ppm. Blue dagger: 1,2- $^{13}$ C<sub>2</sub> squarate signals; Magenta double-dagger: 1,3- $^{13}$ C<sub>2</sub> squarate signals. (a) A 90° pulse-acquire  $^{13}$ C NMR spectrum of the  $^{13}$ C<sub>1</sub>-squarate solution in a magnetic field of 9.4 T, averaged over 512 transients. (b) Double-quantum filtered spectrum obtained using the GeoDQ pulse sequence (1024 transients at 16.4 T), using parameters optimised for 1,2- $^{13}$ C<sub>2</sub>-squarate (see Table III). (c) Singlet-filtered spectrum obtained using the GeoDQ-singlet pulse sequence (1024 transients at 16.4 T). The vertical scales of (b) and (c) are identical. The signal intensities of (a) cannot be compared directly with those of (b) and (c).

trajectory on the Bloch sphere of the zero-quantum transition, with an opening angle of  $\pi/2$ , so that the trajectory subtends a solid angle of  $\pi$  at the origin<sup>47</sup>. This geometrical property invests the connected single-quantum coherences with opposite phase shifts of  $\pm \pi/2$ , permitting the excitation of double-quantum coherence by a subsequent  $\pi/2$  pulse<sup>47</sup>. The phase shift of the  $|T_0\rangle$  state induced by the  $\Pi_z^{\rm ZQ}$  sequence, which is associated with the solid angle subtended by the zero-quantum Bloch-sphere trajectory, is a manifestation of the geometric Aharanov-Anandan phase<sup>47,56</sup>, a non-adiabatic generalisation of Berry's phase<sup>57,58</sup>.

The timings of the GeoDQ sequence depend on the parameters  $\Omega$  and  $\theta_{ST}$ , which are defined as follows in terms of the parameters of the near-equivalent spin-1/2

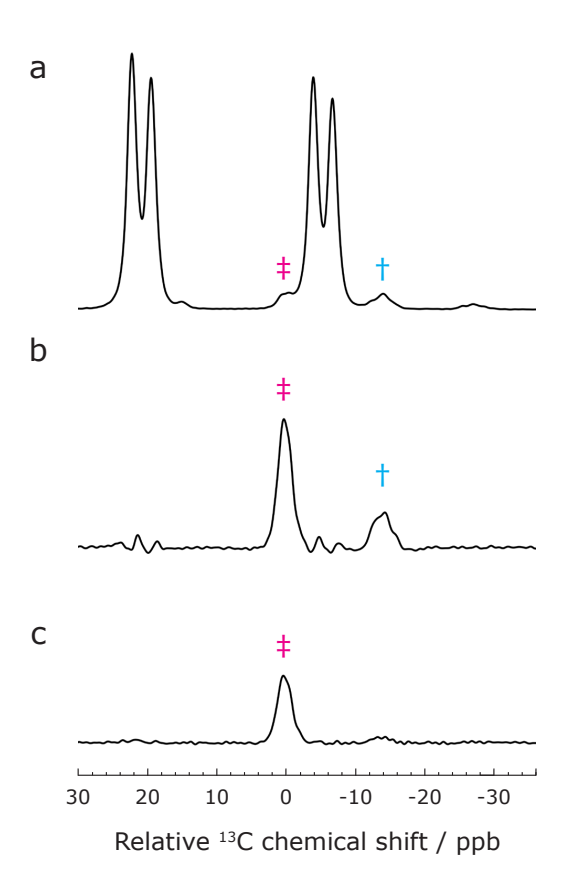


Figure 10. Selective  $^{13}\mathrm{C}$  NMR of 1,3- $^{13}\mathrm{C}_2$ -squarate. All spectra are for a solution of  $^{13}\mathrm{C}_1$  squarate at pH 13.3 and 298 K. The chemical shift scale is centred at 203.05 ppm. Blue dagger: 1,2- $^{13}\mathrm{C}_2$  squarate signals; Magenta double-dagger: 1,3- $^{13}\mathrm{C}_2$  squarate signals. (a) A 90° pulse-acquire  $^{13}\mathrm{C}$  NMR spectrum of the  $^{13}\mathrm{C}_1$ -squarate solution in a magnetic field of 9.4 T, averaged over 512 transients. (b) Double-quantum filtered spectrum obtained using the GeoDQ pulse sequence (1024 transients at 16.4 T), using parameters optimised for 1,3- $^{13}\mathrm{C}_2$ -squarate (see Table III). (c) Singlet-filtered spectrum obtained using the GeoDQ-singlet pulse sequence (1024 transients at 16.4 T). The vertical scales of (b) and (c) are identical. The signal intensities of (a) cannot be compared directly with those of (b) and (c).

pair:

$$\Omega = \sqrt{\omega_J^2 + \omega_\Delta^2},$$

$$\theta_{ST} = \arctan\left(\frac{\omega_\Delta}{\omega_J}\right).$$
(6)

The chemical shift frequency difference  $\omega_{\Delta}$  and Jcoupling are given in angular units by

$$\omega_{\Delta} = \Delta \delta \times \omega^{0},$$
  

$$\omega_{J} = 2\pi J,$$
(7)

where  $\Delta \delta$  is the difference in chemical shifts and  $\omega^0 = -\gamma B^0$  is the nuclear Larmor frequency of the homonu-

clear spin pair. The angle  $\theta_{\rm ST}$  is the singlet-triplet mixing angle, and is small in magnitude for a near-equivalent AB system, approaching  $\pi/2$  for the weak-coupling AX case. The current spin systems all have small values of  $\theta_{\rm ST}$ , as shown in Table III.

Theoretical expressions for the pulse sequence intervals  $\tau_1$  and  $\tau_2$ , and the loop number n, are given by  $^{47}$ :

$$\tau_1 = \pi/(2\Omega),$$

$$\tau_2 = 2\tau_1,$$

$$n = 2 \times \text{round}(\pi/(4\theta_{\text{ST}})).$$
(8)

The last equation ensures that n is an even number, which leads to the most robust performance<sup>59</sup>. In practice, these parameters were optimised experimentally. The experimental parameters are given in Table III.

A double-quantum-filtered <sup>13</sup>C NMR spectrum of the <sup>18</sup>O-enriched 1-<sup>13</sup>C squarate solution at high pH is shown in Figure 9(b). This spectrum was obtained using the geometric double-quantum-filtering pulse sequence of Figure 8, using the parameters of Table III (centre column), which are optimised for the detection of the 1,2-<sup>13</sup>C<sub>2</sub>-squarate isotopologue. As may be seen in Figure 9(b), the selective detection of the small 1,2-<sup>13</sup>C<sub>2</sub>-squarate signal, and the suppression of the large <sup>13</sup>C<sub>1</sub> signals, is excellent.

Figure 10(b) shows a similar spectrum, obtained by using the parameters of Table III (right column), which are optimised for the detection of the  $1,3^{-13}C_2$ -squarate isotopologue. In this case, the  $1,3^{-13}C_2$ -squarate signal is observed with high efficiency. The  $1,2^{-13}C_2$ -squarate signal also appears in this spectrum, albeit with reduced intensity. This is expected, since the double-quantum filter allows signals of both  $^{13}C_2$  pairs to pass. The suppression of the  $^{13}C_1$  signals is excellent in this case too.

# C. Double-Quantum Filtered Singlet NMR

Geometric double-quantum filtration may be combined with singlet NMR, in order to assess the singlet relaxation of the 1,2- $^{13}\mathrm{C}_2$  squarate and 1,3- $^{13}\mathrm{C}_2$ -squarate isotopologues, without interference from the much larger signals of the  $^{13}\mathrm{C}_1$  species.

The complete pulse sequence for double-quantumfiltered singlet NMR is shown in Figure 11. The pulse sequence consists of eight consecutive elements:

- (i) Singlet-order-destruction (SOD). Longitudinal magnetization and singlet order are destroyed using a sequence of radio-frequency pulses, delays, and field gradient pulses<sup>21</sup>. The SOD sequence used in the current experiments is specified in the Supplementary Information.
- (ii) Geometric Double-Quantum Excitation. After a delay for the establishment of longitudinal magnetisation, a geometric double-quantum excitation sequence generates  $^{13}\mathrm{C}_2$  double-quantum coherence.

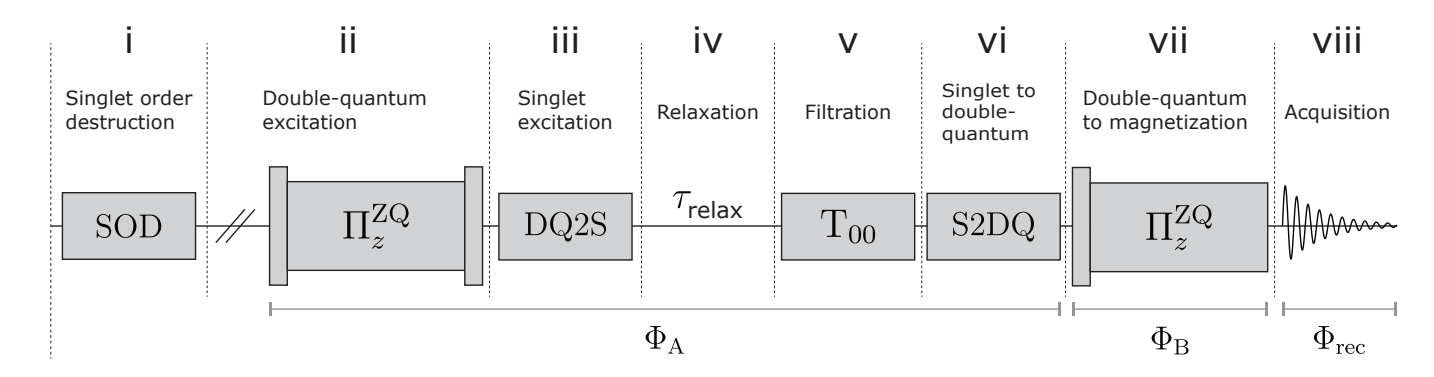


Figure 11. Geometric double-quantum-filtering singlet pulse sequence. The pulse sequence elements are as follows: (i) The singlet-order destruction (SOD) block<sup>21</sup> removes any longitudinal magnetization and residual singlet order. (ii) Following a relaxation delay to establish longitudinal magnetization, double-quantum coherence is generated by a geometric double-quantum excitation block, with an overall phase shift  $\Phi_A$ . (iii) A double-quantum-to-singlet (DQ2S) block converts double-quantum coherence to singlet order. (iv) Singlet order decays during the relaxation interval  $\tau_S$ . (v) A  $T_{00}$  filter removes signals which do not pass through any rank-0 spherical tensor operators. (vi) A singlet-to-double-quantum (S2DQ) block converts singlet order to double-quantum coherence. (vii) A second geometric double-quantum pulse block is applied, with an overall phase  $\Phi_B$ . (viii) The NMR signal is acquired and digitized, with receiver phase  $\Phi_{rec}$ . The phases of the blocks are cycled as an overall four-step cycle:  $\Phi_A = \{0, 0, 0, 0\}$ ,  $\Phi_B = \{0, \pi/2, \pi, 3\pi/2\}$  and  $\Phi_{rec} = \{0, 3\pi/2, \pi, \pi/2\}$ .

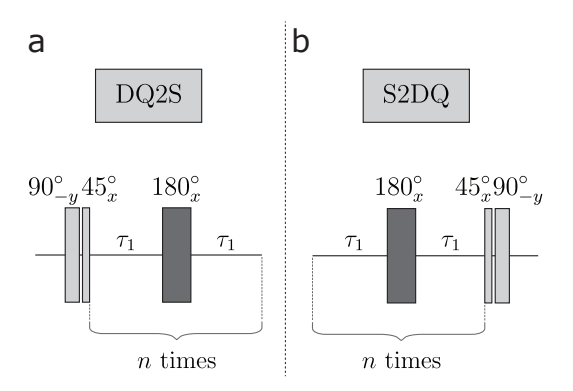


Figure 12. (a) The double-quantum to singlet (DQ2S) block converts double-quantum coherence into singlet order. (b) The singlet to double-quantum (S2DQ) block is the chronological reverse of the DQ2S block, and converts singlet order back to double-quantum coherence. The darker colour indicates the implementation of a composite 180° pulse<sup>53</sup>. The parameters used in the experiments are given in Table III.

The sequence used is given in Figure 8, with the parameters for 1,2-<sup>13</sup>C<sub>2</sub> and 1,3-<sup>13</sup>C<sub>2</sub> squarate specified in Table III.

- (iii) Double-Quantum-To-Singlet Conversion (DQ2S). This pulse sequence block is shown in Figure 12(a). This consists of an initial π/2 pulse with phase -π/2, followed by a π/4 pulse with phase 0, followed by a J-synchronized spin echo sequence, of similar type to that used in the M2S pulse sequence for converting longitudinal magnetization into singlet order<sup>8</sup>. The operation of this sequence is described below.
- (iv) The singlet order is allowed to decay for a variable

interval  $\tau_{\rm relax}$ .

- (v) A T<sub>00</sub> filter block suppresses all signals that do not pass through rank-0 spherical tensor order<sup>15,24</sup>. Since singlet order is described by a rank-0 spherical tensor operator, signals deriving from <sup>13</sup>C<sub>2</sub> singlet order pass through the filter, while spurious signals from magnetization components are suppressed. The sequence used in the current experiments is specified in the Supplementary Information.
- (vi) A Singlet-To-Double-Quantum (S2DQ) sequence converts singlet order back into double-quantum coherence. This pulse sequence block is shown in Figure 12(b), and is the chronological reverse of the DQ2S sequence.
- (vii) A second geometric double-quantum sequence converts the double-quantum coherence into observable transverse magnetization. The sequences used are as in Figure 8. The pulse sequence parameters for 1,2-<sup>13</sup>C<sub>2</sub> and 1,3-<sup>13</sup>C<sub>2</sub>-squarate are specified in Table III.
- (viii) The  $^{13}{\rm C}$  NMR signal is observed with a receiver phase  $\Phi_{\rm rec}.$

The phases  $\Phi_A$  and  $\Phi_B$  of the pulse sequence blocks, and the receiver phase  $\Phi_{\rm rec},$  are cycled in subsequent transients, in order to suppress signals that do not pass through  $^{13}C_2$  double-quantum coherences. The relaxation interval  $\tau_{\rm relax}$  is varied in a series of experiments in order to study the decay of  $^{13}C_2$  singlet order in the two isotopomers.

The DQ2S pulse sequence block is shown in Figure 12(a). The theoretical values of  $\tau_1$  and n are as given

in Equation 8. The experimentally optimised values are given in Table III.

The sequence operates as follows: The double-quantum spin density operator, generated by the GeoDQ sequence, has the following form (omitting the unity operator and numerical factors) <sup>47</sup>:

$$\rho_0 = i |T_{-1}\rangle \langle T_{+1}| - i |T_{+1}\rangle \langle T_{-1}|. \tag{9}$$

This has the following matrix representation, in the basis of singlet and triplet states (Equation 1):

$$\rho_0 = i \begin{pmatrix} 0 & 0 & 0 & 0 \\ 0 & 0 & 0 & -1 \\ 0 & 0 & 0 & 0 \\ 0 & +1 & 0 & 0 \end{pmatrix}. \tag{10}$$

The first  $\pi/2$  pulse of the DQ2S block converts the double-quantum coherence into antiphase triplet-triplet coherence:

$$\rho_1 = R_y(-\pi/2)\rho_0 R_y(+\pi/2) = \frac{i}{\sqrt{2}} \begin{pmatrix} 0 & 0 & 0 & 0\\ 0 & 0 & -1 & 0\\ 0 & +1 & 0 & +1\\ 0 & 0 & -1 & 0 \end{pmatrix}.$$
(11)

The  $\pi/4$  pulse converts this into a state in which the central triplet state has a depleted population, relative to the two outer triplet states:

$$\rho_2 = R_x(\pi/4)\rho_1 R_x(-\pi/4) = \frac{1}{2} \begin{pmatrix} 0 & 0 & 0 & 0 \\ 0 & +1 & 0 & +1 \\ 0 & 0 & -2 & 0 \\ 0 & +1 & 0 & +1 \end{pmatrix}.$$
(12)

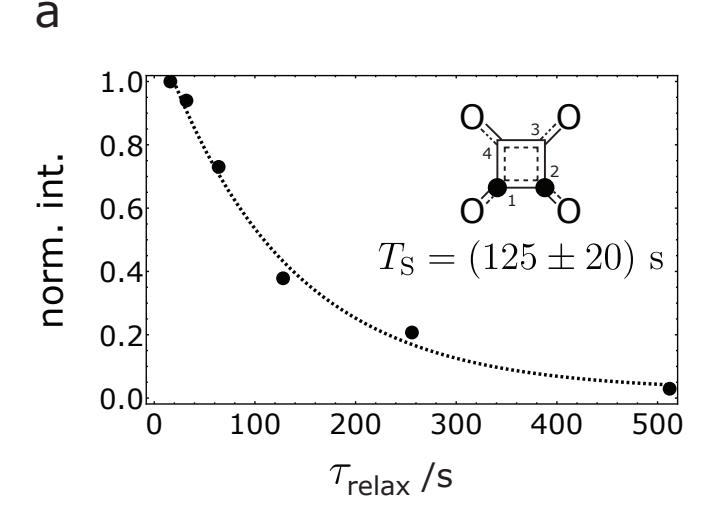
The next element of the DQ2S sequence is a J-synchronised multiple spin echo sequence, as shown in Figure 12(a). The intervals  $\tau_1$  are given in Equation 8.

As described in several places<sup>8,11</sup>, a J-synchronized spin echo sequence of suitable duration induces a rotation through  $\pi$  about the x-axis of the zero-quantum subspace spanned by the  $|S_0\rangle$ ,  $|T_0\rangle$  states. This transformation exchanges the populations of the singlet and central triplet states, leading to the following density operator:

$$\rho_3 = R_x^{\text{ZQ}}(\pi)\rho_2 R_x^{\text{ZQ}}(-\pi) = \frac{1}{2} \begin{pmatrix} -2 & 0 & 0 & 0\\ 0 & +1 & 0 & +1\\ 0 & 0 & 0 & 0\\ 0 & +1 & 0 & +1 \end{pmatrix}.$$
(13)

The state  $\rho_3$  contains a component of singlet order, since the mean population of the three triplet states (=1/3) differs from the population of the singlet state (=-1). Hence, the sequence of manipulations in Figure 12(a) converts double-quantum coherence into singlet order. The reverse sequence S2DQ (Figure 12(b)) accomplishes the opposite transformation.

The overall theoretical efficiency for the DQ2S/S2DQ sequences to convert double-quantum coherence into sin-



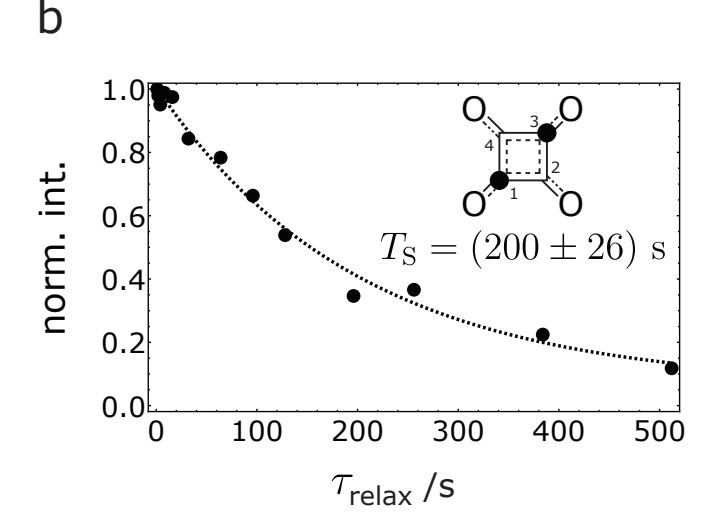


Figure 13. (a) Decay curve for the  $^{13}\mathrm{C}_2$  singlet order of the  $^{13}\mathrm{C}_2$ -squarate isotopologue. (b) Decay curve for the  $^{13}\mathrm{C}_2$ -singlet order of the  $^{13}\mathrm{C}_2$ -squarate isotopologue. All results were obtained on a degassed solution of  $^{13}\mathrm{C}_1$ -squarate in a field of 16.4 T at a temperature of 298 K, using the double-quantum-filtered singlet pulse sequence in Figure 11. The dotted lines are best fits to single-exponential decays of the signal intensities.

glet order, and back to double-quantum coherence again, is 2/3. This is the maximum achievable by consecutive unitary transformations<sup>60,61</sup>.

Figures 9(c) and 10(c) show  $^{13}\mathrm{C}$  NMR spectra acquired by using the pulse sequence in Figure 11, but with no relaxation delays  $\tau_{\mathrm{relax}}$ . These NMR signals derive from the  $^{13}\mathrm{C}$  magnetization of the  $^{13}\mathrm{C}_2$ -squarate isotopologues which have passed through both double-quantum coherence and singlet order. The sequences are seen to be highly selective and efficient. The nuclear spin order of the  $^{13}\mathrm{C}_2$  pairs passes through double-quantum coherence to singlet order, and back again, with the retained amplitude not greatly less than the theoretical bound of 2/3.

#### D. Relaxation Measurements

The relaxation interval  $\tau_{\rm relax}$  of the pulse sequence in Figure 11 was varied in a series of experiments in order to study the decay of  $^{13}{\rm C}_2$  singlet order in the two isotopomers. Results obtained on a degassed solution at a magnetic field of 16.4 T are shown in Figure 13. The  $^{13}{\rm C}_2$  singlet decay of the 1,2- $^{13}{\rm C}_2$ -squarate isotopologue ( $T_S \simeq 125 \pm 20\,{\rm s}$ ) is faster than that of the 1,3- $^{13}{\rm C}_2$ -squarate isotopologue ( $T_S \simeq 200 \pm 26\,{\rm s}$ ). This observation is in line with the molecular inversion symmetry of the 1,3- $^{13}{\rm C}_2$ -squarate isotopologue, which cancels out the chemical shift anisotropy mechanism.

The singlet decay may be compared with the  $T_1$  values for the decay of longitudinal magnetization for the same isotopologues, which were estimated by using a standard inversion-recovery sequence followed by geometric double-quantum filtration, in order to selectively observe the relaxation of the  $1,2^{-13}C_2$  or  $1,3^{-13}C_2$ -squarate signals. The observed  $T_1$  values were  $29\pm1\,\mathrm{s}$  in both cases, indicating that the singlet order decay is between 6 and 10 times slower than that of the longitudinal magnetization for the species.

#### IV. DISCUSSION

The squarate dianion presents an unusual example of high local symmetry and the absence of magnetic nuclei in the most abundant natural isotopologue. By synthetically introducing a single  $^{13}\mathrm{C}$  label into each molecule, and using double-quantum techniques, it is possible to study low-abundance  $^{13}\mathrm{C}_2$  isotopologues in which the  $^{13}\mathrm{C}$  nuclei are either at adjacent molecular positions (in the case of 1,2- $^{13}\mathrm{C}_2$ -squarate) or at inversion-related molecular positions (in the case of 1,3- $^{13}\mathrm{C}_2$ -squarate). Long-lived  $^{13}\mathrm{C}_2$  singlet order may be accessed in these isotopologues by introducing  $^{18}\mathrm{O}$  nuclei, which have no magnetic moment but which slightly modify the  $^{13}\mathrm{C}$  chemical shifts through the mass difference between  $^{16}\mathrm{O}$  and  $^{18}\mathrm{O}$ .

The <sup>13</sup>C NMR spectrum of <sup>18</sup>O-enriched <sup>13</sup>C-squarate presents a rich multiplet structure, due to the large number of isotopologues and the plethora of secondary isotope shifts. The <sup>18</sup>O-induced <sup>13</sup>C isotope shifts are observed to be strongly pH-dependent. These pH-dependent isotope shifts are attributed to a superposition of the vibronic and dynamic isotope shift mechanisms. In the dynamic mechanism, the substitution of an <sup>16</sup>O atom by an <sup>18</sup>O atom at a molecular protonation site perturbs the average <sup>13</sup>C chemical shifts throughout the molecule by slightly shifting the acid-base equilibrium.

At high pH the dynamic contribution to the isotope shifts vanishes since the squarate dianion  $C_4O_4^{2-}$  is the only significant species in solution. The remaining vibronic shifts display an unexpected property: the two-bond  $^2\Delta^{13}C(^{18}O)$  secondary isotope shift is negligibly small, unlike both the one-bond shift  $^1\Delta^{13}C(^{18}O)$  and the three-bond shift  $^3\Delta^{13}C(^{18}O)$ . The very small value

of the two-bond isotope shift is unexplained at the current time.

The  $^{18}{\rm O}$ -induced  $^{13}{\rm C}$  isotope shifts allow the use of geometric double-quantum-filtering to selectively detect the signals from the minor  $1,2^{-13}{\rm C}_2$  and  $1,3^{-13}{\rm C}_2$ -squarate isotopologues, with good suppression of the much larger signals from the  $^{13}{\rm C}_1$  species. The conversion of  $^{13}{\rm C}_2$  double-quantum coherence into  $^{13}{\rm C}_2$  singlet order, and back again, was demonstrated with good efficiency, by using novel DQ2S and S2DQ procedures.

As expected, the singlet relaxation time constants  $T_S$ were found to greatly exceed the  $T_1$  values, for both the  $1,2^{-13}C_2$ -squarate and the  $1,3^{-13}C_2$ -squarate isotopologues. The  $T_S$  time constant for 1,3-13 $C_2$ -squarate was measured to be  $\sim 200\,\mathrm{s}$  in high-pH aqueous solution, in the high magnetic field of 16.4 T. The long singlet relaxation time may be attributed to the inversion symmetry of this molecular species, which causes excellent suppression of the large chemical shift anisotropy mechanism, even in high magnetic field. Nevertheless, although the  $T_S$  time constant is unusually long for a species in high magnetic field in aqueous solution, it seems that intermolecular interactions with solvent protons and other species, combined with the relatively high viscosity of the aqueous environment, still limit the singlet relaxation time to a few minutes, even for this highly favourable species.

### SUPPLEMENTARY INFORMATION

The supplementary information contains: (1) computational chemistry calculations of the CSA tensors and the *J*-couplings; (2) additional pulse sequence details.

### **ACKNOWLEDGEMENTS**

We acknowledge funding from the European Research Council (Grant No. 786707-FunMagResBeacons) and EPSRC-UK (Grant Numbers EP/P030491/1, and EP/V055593/1).

# **AUTHOR DECLARATIONS**

# Conflicts of Interest

The authors have no conflicts to disclose.

# **AUTHOR CONTRIBUTIONS**

Urvashi D. Heramun: Investigation (lead); Data curation (equal); Visualization (lead); Validation (equal); Formal analysis (equal); Writing – original draft (equal); Writing – review & editing (equal). Mohamed Sabba:

Conceptualization (equal); Methodology (equal); Validation (equal); Supervision (supporting); Formal analysis (supporting); Writing – review & editing (supporting). Christian Bengs: Conceptualization (equal); Methodology (equal); Validation (equal); Supervision (supporting); Formal analysis (supporting); Software (equal); Writing – review & editing (supporting). Gamal Moustafa: Resources (lead). Malcolm H. Levitt: Conceptualization (equal); Data curation (equal); Formal analysis (equal); Funding acquisition (lead); Validation (equal); Project administration (lead); Software (equal); Supervision (lead); Writing – review & editing (equal); Writing – original draft (equal).

### DATA AVAILABILITY STATEMENT

The data that support the findings of this study are available from the corresponding author upon reasonable request. The pulse sequences used were deposited and made available with the assigned DOI: https://doi.org/10.5258/SOTON/D3557.

### **REFERENCES**

- $^1\mathrm{M}.$  Carravetta, O. G. Johannessen, and M. H. Levitt, Phys. Rev. Lett.  $\mathbf{92},\ 153003\ (2004).$
- <sup>2</sup>M. Carravetta and M. H. Levitt, J. Am. Chem. Soc. **126**, 6228 (2004).
- <sup>3</sup>S. Cavadini, J. Dittmer, S. Antonijevic, and G. Bodenhausen, J. Am. Chem. Soc. **127**, 15744 (2005).
- <sup>4</sup>G. Pileio, M. Concistrè, M. Carravetta, and M. H. Levitt, Journal of Magnetic Resonance **182**, 353 (2006).
- <sup>5</sup>E. Vinogradov and A. K. Grant, J. Magn. Reson. **188**, 176 (2007).
- <sup>6</sup>P. Ahuja, R. Sarkar, P. R. Vasos, and G. Bodenhausen, J. Chem. Phys. **127**, 134112 (2007).
- <sup>7</sup>W. S. Warren, E. Jenista, R. T. Branca, and X. Chen, Science **323**, 1711 (2009).
- <sup>8</sup>G. Pileio, M. Carravetta, and M. H. Levitt, Proc. Natl. Acad. Sci. U.S.A. **107**, 17135 (2010).
- <sup>9</sup>G. Pileio and M. H. Levitt, J. Chem. Phys. **130**, 214501 (2009).
- <sup>10</sup>G. Pileio, Progress in Nuclear Magnetic Resonance Spectroscopy 56, 217 (2010).
- <sup>11</sup>M. C. D. Tayler and M. H. Levitt, Phys. Chem. Chem. Phys. **13**, 5556 (2011).
- <sup>12</sup>G. Pileio, J. T. Hill-Cousins, S. Mitchell, I. Kuprov, L. J. Brown, R. C. D. Brown, and M. H. Levitt, J. Am. Chem. Soc. **134**, 17494 (2012).
- <sup>13</sup>M. H. Levitt, Annu. Rev. Phys. Chem. **63**, 89 (2012).
- <sup>14</sup>S. J. DeVience, R. L. Walsworth, and M. S. Rosen, Phys. Rev. Lett. **111**, 173002 (2013).
- <sup>15</sup>M. C. D. Tayler and M. H. Levitt, J. Am. Chem. Soc. **135**, 2120 (2013).
- <sup>16</sup> J.-N. Dumez, P. Håkansson, S. Mamone, B. Meier, G. Stevanato, J. T. Hill-Cousins, S. S. Roy, R. C. D. Brown, G. Pileio, and M. H. Levitt, J. Chem. Phys. **142**, 044506 (2015).
- <sup>17</sup>G. Stevanato, S. Singha Roy, J. Hill-Cousins, I. Kuprov, L. J. Brown, R. C. D. Brown, G. Pileio, and M. H. Levitt, Phys. Chem. Chem. Phys. 17, 5913 (2015).
- <sup>18</sup>G. Stevanato, J. T. Hill-Cousins, P. Håkansson, S. S. Roy, L. J. Brown, R. C. D. Brown, G. Pileio, and M. H. Levitt, Angew Chem Int Ed **54**, 3740 (2015).
- <sup>19</sup>S. J. Elliott, L. J. Brown, J.-N. Dumez, and M. H. Levitt, J. Magn. Reson. **272**, 87 (2016).

- $^{20}\mathrm{M}$ . H. Levitt, Journal of Magnetic Resonance **306**, 69 (2019).
- <sup>21</sup>B. A. Rodin, K. F. Sheberstov, A. S. Kiryutin, L. J. Brown, R. C. D. Brown, M. Sabba, M. H. Levitt, A. V. Yurkovskaya, and K. L. Ivanov, J. Chem. Phys. **151**, 234203 (2019).
- $^{22} \rm{J.-N.}$  Dumez, Mol. Phys.  ${\bf 118},\,e1644382$  (2020).
- <sup>23</sup>S. Mamone, N. Rezaei-Ghaleh, F. Opazo, C. Griesinger, and S. Glöggler, Sci. Adv. 6, eaaz1955 (2020).
- <sup>24</sup>M. C. D. Tayler, in *Long-Lived Nuclear Spin Order: Theory and Applications*, edited by G. Pileio (Royal Society of Chemistry, 2020) pp. 188–208.
- <sup>25</sup>C. Bengs, L. Dagys, G. A. I. Moustafa, J. W. Whipham, M. Sabba, A. S. Kiryutin, K. L. Ivanov, and M. H. Levitt, J. Chem. Phys. **155**, 124311 (2021).
- <sup>26</sup>J. Eills, E. Cavallari, R. Kircher, G. D. Matteo, C. Carrera, L. Dagys, M. H. Levitt, K. L. Ivanov, S. Aime, F. Reineri, K. Münnemann, D. Budker, G. Buntkowsky, and S. Knecht, Angew. Chem. Int. Ed. **60**, 6791 (2021).
- <sup>27</sup>S. Mamone, A. B. Schmidt, N. Schwaderlapp, T. Lange, D. von Elverfeldt, J. Hennig, and S. Glöggler, NMR Biomed. **34**, e4400 (2021).
- <sup>28</sup>A. Sonnefeld, A. Razanahoera, P. Pelupessy, G. Bodenhausen, and K. Sheberstov, Sci. Adv. 8, eade2113 (2022).
- <sup>29</sup>X. Yang, K.-R. Hu, J.-X. Xin, Y.-X. Li, G. Yang, D.-X. Wei, and Y.-F. Yao, Journal of Magnetic Resonance **338**, 107188 (2022).
- <sup>30</sup>A. Razanahoera, A. Sonnefeld, G. Bodenhausen, and K. Sheberstov, Magn. Reson. 4, 47 (2023).
- <sup>31</sup>D. H. Lysak, F. V. C. Kock, S. Mamone, R. Soong, S. Glöggler, and A. J. Simpson, Chem. Sci. 14, 1413 (2023).
- <sup>32</sup>H. Harbor-Collins, M. Sabba, C. Bengs, G. Moustafa, M. Leutzsch, and M. H. Levitt, The Journal of Chemical Physics 160, 014305 (2024).
- <sup>33</sup> J. W. Whipham, M. Sabba, L. Dagys, G. Moustafa, C. Bengs, and M. H. Levitt, The Journal of Chemical Physics 161, 014112 (2024).
- <sup>34</sup>P. R. Bunker and P. Jensen, Fundamentals of Molecular Symmetry (Institute of Physics, Bristol, 2005).
- <sup>35</sup>R. Radeglia, Solid State Nuclear Magnetic Resonance 4, 317 (1995).
- <sup>36</sup>R. P. Young, C. R. Lewis, C. Yang, L. Wang, J. K. Harper, and L. J. Mueller, Magn. Reson. Chem. **57**, 211 (2019).
- <sup>37</sup>A. D. Buckingham and S. M. Malm, Mol. Phys. **22**, 1127 (1971).
- $^{38}{\rm N.~F.}$  Ramsey, Phys. Rev.  ${\bf 87},\,1075$  (1952).
- <sup>39</sup>H. Batiz-Hernandez and R. Bernheim, Progress in Nuclear Magnetic Resonance Spectroscopy 3, 63 (1967).
- $^{40}$ C. J. Jameson, J. Chem. Phys. **66**, 4983 (1977).
- <sup>41</sup>P. E. Hansen, Progress in Nuclear Magnetic Resonance Spectroscopy 20, 207 (1988).
- <sup>42</sup>C. J. Jameson, in *Isotopes in the Physical and Biomedical Science*, Vol. 2 (Elsevier Science, Amsterdam, Netherlands, 1991).
- <sup>43</sup>P. Lantto, S. Kangasvieri, and J. Vaara, The Journal of Chemical Physics 137, 214309 (2012).
- <sup>44</sup>P. Lantto, S. Kangasvieri, and J. Vaara, Phys. Chem. Chem. Phys. **15**, 17468 (2013).
- <sup>45</sup> A. Bax, R. Freeman, and S. P. Kempsell, J. Am. Chem. Soc. 102, 4849 (1980).
- <sup>46</sup>T. Nakai and C. A. Mcdowell, Mol. Phys. **79**, 965 (1993).
- <sup>47</sup>C. Bengs, M. Sabba, and M. H. Levitt, J. Chem. Phys. **158**, 124204 (2023).
- <sup>48</sup>S. L. R. Ellison and M. J. T. Robinson, J. Chem. Soc. Chem. Commun. **0**, 745 (1983).
- <sup>49</sup>C. L. Perrin and J. D. Thoburn, J. Am. Chem. Soc. **114**, 8559 (1992).
- <sup>50</sup>W. Arias and J. M. Risley, J. Org. Chem. **56**, 3741 (1991).
- <sup>51</sup>T. L. Mega and R. L. Van Etten, J. Am. Chem. Soc. **115**, 12056 (1993).
- <sup>52</sup>B. N. Craig, M. U. Janssen, B. M. Wickersham, D. M. Rabb, P. S. Chang, and D. J. O'Leary, J. Org. Chem. **61**, 9610 (1996).
- <sup>53</sup>M. H. Levitt and R. Freeman, J. Magn. Reson. 33, 473 (1979).
- <sup>54</sup> A. Bax, R. Freeman, T. A. Frenkiel, and M. H. Levitt, J. Magn. Reson. **43**, 478 (1981).

- $^{55}\mathrm{S.}$  J. De Vience, R. L. Walsworth,  $% \mathrm{S.}$  and M. S. Rosen, NMR in
- Biomedicine **26**, 1204 (2013).  $^{56}$ Y. Aharonov and J. Anandan, Phys. Rev. Lett. **58**, 1593 (1987).
- $^{57}\mathrm{M}.$  Berry, Proc. R. Soc. Lond. A  $392,\,45$  (1984).  $^{58}\mathrm{J}.$  W. Zwanziger, M. Koenig, and A. Pines, Annu. Rev. Phys. Chem. **41**, 601 (1990).
- $^{59}\mathrm{M.}$  C. D. Tayler, Theory and Practice of Singlet Nuclear Magnetic Resonance, Ph.D. thesis, University of Southampton
- <sup>60</sup>O. W. Sørensen, J. Magn. Reson. 1969 86, 435 (1990).
   <sup>61</sup>M. H. Levitt, Journal of Magnetic Resonance 262, 91 (2016).